



2020 Kyoto Japan

Oso Landslide: Failure Mechanism and Runout Analyses

Timothy D. Stark and Zhengdan Xu

Abstract

This paper describes and explains the large mobility of the 2014 Oso Landslide, which caused significant fatal consequences. This landslide occurred in two phases, characterized by significantly different material behaviour, strengths, and runout. A portion of the first phase underwent significant undrained strength loss (liquefaction) and travelled over 1.7 km over a nearly horizontal valley surface and devastated a residential community. The second phase underwent brittle failure with much less strength loss and runout than the first phase. The first phase slide mass is composed of insensitive, overconsolidated glaciolacustrine silt and clay, material not traditionally recognized as susceptible to a large undrained strength loss or liquefaction. A new rheology, appropriate for liquefied overconsolidated glaciolacustrine silt and clay, is presented and used in the runout analyses. The large runout occurred in two directions, which allows various runout models to be compared. Three numerical runout models were used to investigate their applicability to similar landslide configurations and future hazard and risk assessments. These runout analyses show the importance of: (1) using a digital terrain model in the runout analysis, (2) modeling field representative shear strength properties and failure mechanisms, and (3) predicting runout distance, splash height, and duration for risk assessments and to improve public safety for this and other slopes.

Keywords

Landslide • Runout analysis • Failure mechanism • Stability analyses • Colluvium • Shear strength • Undrained strength loss • LiDAR

Landslide Overview

On 22 March 2014 a large and fast moving landslide destroyed the Steelhead Haven Community near Oso, Washington along the North Fork of the Stillaguamish River in Snohomish County. This landslide is considered the deadliest in the history of the continental U.S. with 43 fatalities (Wartman et al. 2016). The entire landslide involved approximately 8.3 million cubic meters of glacial deposits and water filled colluvium from prior landslides present along the slope toe. The colluvium-derived flowslide travelled more than 1.7 km to its distal edge on the south side of SR530 that connects Oso and Darrington, Washington. During various site visits (May 22 through 24, 2014; February 28, 2015; April 16, 2015), the first author examined various landslide features and exposed geology, obtained soil samples for laboratory testing to estimate engineering properties, reviewed aerial photographs, and conducted stability analyses to assess the impact of changes in slope geometry with time. This paper summarizes the material properties measured during the investigation, the resulting two phase failure mechanism, and accompanying runout analyses.

T. D. Stark (✉)

Dept. of Civil Engineering, University of Illinois At Urbana-Champaign, 205 N. Mathews Ave, Urbana, IL 60801, USA

e-mail: tstark@illinois.edu

Z. Xu

Hong Kong University of Science and Technology, Hong Kong, China

e-mail: zxubv@connect.ust.hk

Subsurface Conditions

The crest of the Oso landslide slope is located at an elevation of approximately 270 m on the north side of the west-trending valley of the Stillaguamish River, which is around elevation 75 m. This corresponds to a slope height of

about 200 m. The width of the Stillaguamish River Valley floor at this location varies from 2.0 km to more than 6.0 km. This slope is part of a large overconsolidated glacial terrace deposit that developed after the last advance of continental glacial ice sheets into the Puget Sound. The 2014 landslide occurred at a relatively narrow reach of the river, where it flows north and then west along the slope toe. The river erosion, especially at the eastern end, has caused a number of landslides in the lower portion of the slope including landslides in 1937, 1951, 1952, 1967, 1988, and 2006, (see 2006 landslide in Fig. 1).

Knowledge of the pre-2014 landslide subsurface conditions is important for understanding the failure mechanism, because a comparison of the initial and final locations of the various glacial soil deposits aided the understanding of landslide initiation, movement, number of phases, and run-out. Based on the exposed landslide headscarp, hand and shovel excavations during various site visits, geologic maps, borings before (Shannon and Associates 1952) and after the landslide (Badger and D'Ignazio 2015), and soil samples collected and tested herein, the subsurface profile prior to the 2014 landslide is shown in Fig. 2 and is located at the cross-section location shown in Fig. 1.

The slope subsurface profile consists of (from top to bottom):

- **Recessional Outwash:** tan to light brown unsaturated cohesionless fluvial deposits, medium dense to dense fine to coarse sands with cross-beddings. The thickness of this outwash is about 40 m from elevation 270 to 230 m. The top of this deposit is referred to locally as the Upper Plateau or Whitman Bench (see Fig. 2).
- **Glacial Till:** light grey unsaturated, stiff to very stiff, overconsolidated, and unsorted mixtures of clay, silt,

sand, and gravels with scattered cobbles and boulders. The thickness of this layer is approximately 23 m from elevation 230 to 207 m.

- **Advanced Outwash:** tan to light brown unsaturated fluvial medium dense coarse sand and sandy gravel with localized clay and silt interbeds. The Advanced Outwash thickness is approximately 30 m from elevation 207 to 177 m.
- **Advanced Glacio-Lacustrine:** light to dark grey, medium stiff to stiff, unsaturated to saturated with horizontally laminated low to high plasticity clays and silts with occasional fine sands laminae. The thickness of this layer is approximately 82 m, from elevation 177 to 95 m, and was also involved in most, if not all, of the prior low elevation landslides caused by river erosion along the slope toe. The unsaturated condition of the Advanced Glacio-Lacustrine deposit is evident in surficial exposures and in available borings.
- **Sands and Gravels:** well sorted fine to medium grained sands and gravel with possible artesian pressures.
- **Fluvial deposits/colluvium:** oxidized deposits of loose saturated sands and silts forming the river floodplain, mixed with debris from prior landslides exposed near base of slope, and is youngest deposit and not part of stratigraphic sequence.

Prior Landslide History

The 2014 landslide occurred in a slope with a history of prior landslides. Modern accounts of landslides in the lower portion of the slope date back to 1932 (Thorsen 1969). More recent high resolution topographic relief images generated by LiDAR (Light Detection and Ranging) show many large prehistoric landslides including one at the location of the 2014 landslide have occurred in this valley (see Fig. 3).

The documented history of landsliding at this site reveals two types of event: (1) large prehistoric landslides that involve the upper glacial terrace deposits, i.e., the Whitman Bench (see Figs. 2 and 3), which are similar to the 2014 landslide, and (2) smaller landslides in the lower portion of the slope between 1932 and 2014 were primarily caused by river erosion. Landslides involving the Whitman Bench exhibit significantly greater runout because of the greater elevation and potential energy of the source material than the low elevation landslides.

The occurrence of a large prehistoric landslide at the location of the 2014 landslide is important because it created the Ancient Landslide Bench shown in Fig. 3 that supported and protected the Whitman Bench from landslides primarily caused by river toe erosion and precipitation. Based on the geometry of neighboring high elevation landslides also

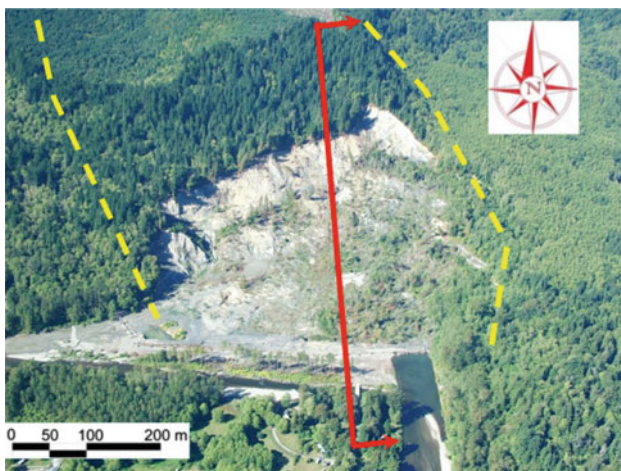


Fig. 1 Aerial view of 2006 landslide, location of cross-section in Fig. 2 (solid line), and outline of sides of 2014 landslide (dashed lines) (image courtesy of Rupert G. Tart)

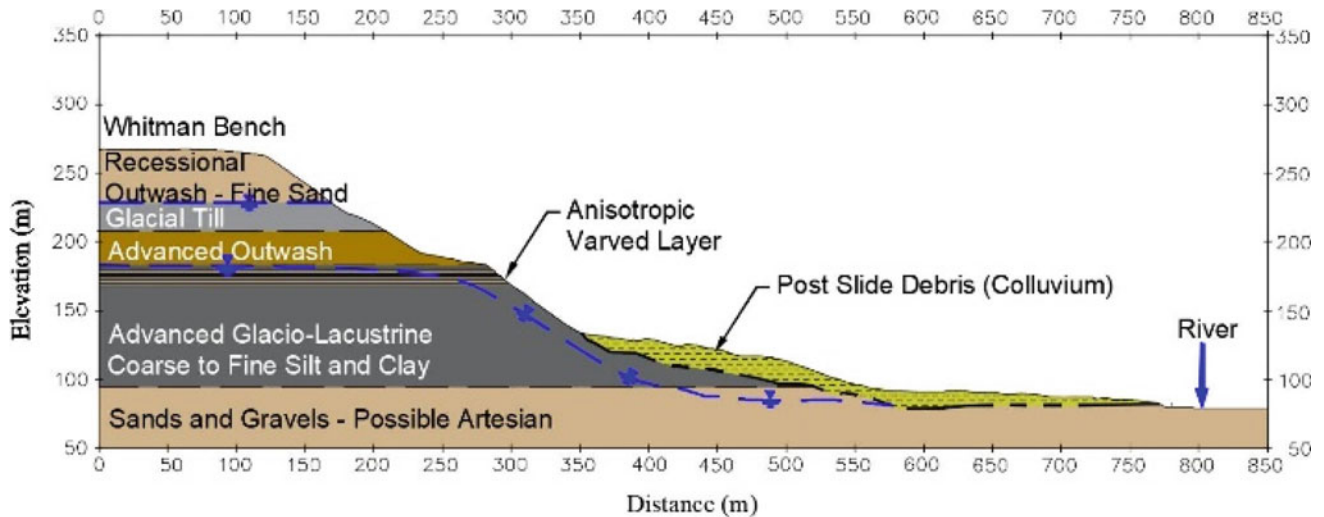


Fig. 2 Slope cross-section at location shown in Fig. 1 prior to 2014 landslide with phreatic surfaces inferred from inverse stability analyses except where observed in borings drilled from the Whitman Bench or in the slide mass

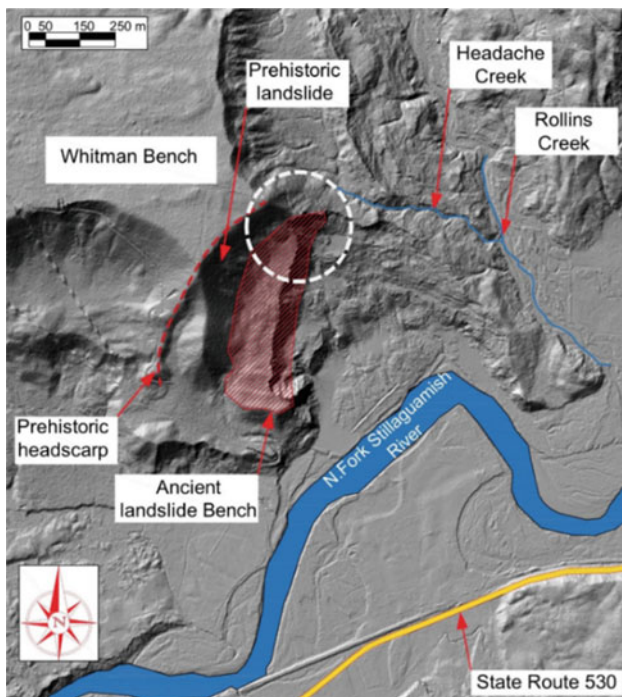


Fig. 3 2013 LiDAR-derived topography showing the Oso landslide in context with the Ancient Landslide Bench (see shaded area) (base courtesy of Puget Sound Lidar Consortium)

shown in Fig. 3, it is anticipated that the ancient landslide at this location occurred through the weak varved lacustrine layers in the upper portion of the Advanced Glacio-Lacustrine deposit and evacuated some of the overlying Whitman Bench. After this landslide, a bench or ledge was created that supported the overlying Whitman Bench slope and protected the Whitman Bench from oversteepening by landslides in the lower portion of the slope until after 2006.

The ancient slide mass travelled down the slope and across the Stillaguamish River, where it was eroded over geologic time. This is easy to visualize because the ancient slide mass consisted primarily of two unsaturated sandy outwash deposits that are quickly eroded by the river as witnessed after the 2014 landslide. During a site visit only two months after the 2014 landslide, a significant amount of these sandy outwash deposits had already been eroded by the Stillaguamish River (see Fig. 3) and exposed the underlying Advanced Glacio-Lacustrine clays. This explains the lack of a significant portion of the ancient slide mass being present on the valley floor prior to the 2006 and 2014 landslides.

Using aerial photographs of the 1937, 1951, 1952, 1967, 1988, and 2006 landslides assembled by the Seattle Times (<https://projects.seattletimes.com/2014/building-toward-disaster/>), Kim et al. (2015) and Sun et al. (2015) show only the lower portion of the slope and the Advanced Glacio-Lacustrine Clay deposits were involved. These low elevation landslides removed some of the Ancient Landslide Bench but there was still sufficient width of the bench to support the overlying Whitman Bench until after the 2006 landslide. The slide masses from these lower elevation landslides accumulated along the slope toe or advanced only 85 m in the 1947 slide, 200 m in the 1967 slide, and 250 m in the 2006 slide from the slope toe, respectively, based on aerial photographs because of their low elevation, low potential energy, and lack of significant strength loss. Nevertheless, in each of these low elevation landslides the slide mass would move the active river channel to the south away from the slope toe. The river would then start eroding the prior landslide debris to the north until it was again undermining the Advanced Glacio-Lacustrine Clays again. Based on the dates of prior landslides and aerial photographs, it

took about 35 to 40 years for the river to erode enough landslide debris/colluvium to initiate another landslide in the lower portion of the slope. Each of these landslides would remove some of the Ancient Landslide Bench especially on the eastern end where the river flowed almost north directly into the slope (see Fig. 3). This timing of 35 to 40 years is important because only eight years elapsed between the 2006 landslide and the large 2014 landslide, not 35 to 40 years, so a different failure mechanism had to be involved in the 2014 landslide.

2014 Landslide

The 2014 landslide is significantly different than the 1937, 1951, 1952, 1967, 1988, and 2006 landslides in the following four main aspects:

- (1) River erosion did not play a significant role because the river channel had been pushed significantly south of the slope toe by the 2006 landslide,
- (2) 2014 landslide occurred only eight years after the 2006 landslide not 35 to 40 years,
- (3) Slide mobility was much greater, resulting in the slide mass travelling more than 1.7 km in comparison to 85 m, 200 m, and 250 m in the 1947, 1967, and 2006 landslides, respectively.
- (4) 2014 slide mass is much larger than the 1937, 1951, 1952, 1967, 1988, and 2006 slide masses.

As a result, a different failure mechanism than river toe erosion had to initiate the 2014 landslide. The first factor considered for the 2014 landslide is precipitation. The 2014 landslide occurred during a dry sunny morning after a period of unusually intense rainfall. Nearby precipitation gauges with 86 years of data indicate that the rainfall during the twenty-one days (March 1 through 21) preceding the landslide was significantly greater than average (Keaton et al. 2014). In particular, these data show the 45-day period before the landslide was wetter than 98% of the same 45-day period in the 86-year historical record (Iverson et al. 2015). Cao et al. (2014) and Henn et al. (2015) show that the cumulative precipitation for the 21 days prior to the 22 March 2014 landslide corresponds to a return period of about 97 years making the 21 days prior to the landslide the wettest (403 mm of rainfall) on record at the Darrington, Washington rain gauge. It is anticipated that this intense rainfall, higher groundwater, and increased runoff along the eastern side of the 2014 landslide mass triggered a landslide that removed the small remaining portion of the Ancient Landslide Bench on the eastern end (see dashed circle in Fig. 3), and undermined the Whitman Bench discussed

below. This resulted in initiation of the 2014 two-phase failure mechanism described below.

Even with a record rainfall in March 2014, the Oso landslide is the only large landslide in the valley and region so this site had a unique feature, i.e., an oversteepened and/or undermined Ancient Landslide Bench on the eastern end. LiDAR images show no other ancient landslide bench in this area was oversteepened and/or undermined to the extent the eastern bench was in Fig. 3.

Phase I Slide Mass

Based on inverse 2D limit equilibrium stability analyses using the software packages SLIDE and SLOPE/W and the soil properties in Stark et al. (2017) that are reproduced in Table 1, Fig. 5 shows the probable failure surface for the initial instability that triggered the first phase (Phase I) of the 2014 two-phase failure mechanism. Table 1 shows the measured drained fully softened and residual strength envelopes for the fine-grained deposits. These strength envelopes are stress-dependent and Table 1 presents the range of effective stress friction angle from low to high normal stress.

The Phase I instability initiated in the eastern portion of the Ancient Landslide Bench slope (see Fig. 3) where the bench had been oversteepened by prior sliding in the lower portion of the slope. The failure surface in Fig. 5 is based on field observations and inverse stability analyses that yielded a factor of safety of about unity (1.0) for a variety of compound failure surfaces and piezometric levels estimated from the inverse analysis of the 2006 landslide.

Compound slip surfaces were primarily considered because of the observed internal distortion of the slide volume during each of the two phases and the differing soil types in the upper portion of the slope, i.e., outwash sands, glacial till, and varved silts and clays in the Advanced Glacio-Lacustrine deposit that contain weak horizontal layers as discussed above. Circular failure surfaces are only applicable to homogeneous soil deposits. However, a circular search also was conducted, which confirmed the critical failure surface is a compound slip surface.

Colluvial Flowslide of Phase I

The important aspect of the Phase I initial slide mass is that it quickly impacted the water filled, softened, and disturbed colluvium that had accumulated along the lower portion of the slope during prior river induced landslides. At the western end of the slope, a 0.9 to 1.2 km² sedimentation pond with a depth of about 4.6 m had been constructed in

Table 1 Input parameters for 2D limit equilibrium slope stability analyses

Description of geologic deposit	Total and saturated unit weights (kN/m ³)	Estimated peak and measured fully softened effective stress friction angles	Measured residual effective stress friction angle
Recessional outwash	20.0	28 ⁰	N/A
glacial till	20.0	35 ⁰	N/A
Advanced outwash	19.0	30 ⁰	N/A
Low plasticity advanced glacio-lacustrine	20.0	34 ⁰ to 25 ⁰	27 ⁰ to 20 ⁰
High plasticity advanced glacio-lacustrine	20.0	32 ⁰ to 21 ⁰	19 ⁰ to 12 ⁰
Sands and gravels	19.0	35 ⁰	N/A
Prior slide debris (Colluvium)	16.5	32 ⁰ to 21 ⁰	19 ⁰ to 12 ⁰

the colluvium after the 2006 landslide to reduce the amount of sediment entering the river due to precipitation, emergent stream(s) and seepage from the slope, and river flooding. Therefore, the colluvium had an abundance of water between the blocks of overconsolidated clay and within the loose matrix of disturbed colluvium filling these interstices. Many of the “intact” clay blocks were likely also at or near saturation. All of this helped produce a fluid or liquefied behavior after it was impacted by the Phase I slide mass, which is described below. The Phase I slide mass was moving rapidly downslope during its descent of about 150 m when it impacted the colluvium causing a large undrained strength loss, which allowed the colluvium to flow across the river and valley. The large undrained strength loss was evident by the runout of over 1.7 km and trees from the upper plateau still being vertical halfway across the valley.

With the large and rapid impact force from the Phase I initial slide mass, the blocky, softened, and water filled colluvium disintegrated into a fluid with the soil particles becoming suspended in a fluid matrix causing a flowslide using the classifications in Hungr et al. (2014). The fluid colluvium then flowed quickly across the valley like a flowslide ahead of the main Phase I slide mass. The rapidity of the flowslide is evident by the burial of vehicles traveling along SR530 near the middle of the valley. Without the large and rapid push of the Phase I initial slide mass, the colluvium would not have undergone this large undrained strength loss because similar colluvium was present prior to the low elevation landslides in 1937, 1951, 1952, 1967, 1988, and 2006 and these slide masses did not flow past the river and across the valley. Therefore, the large-scale and significant undrained strength loss of the colluvial mass

appears to be contingent on a sufficiently large and energetic impulse from above, which was delivered by the Phase I slide mass from the Whitman Bench in 2014 (see Fig. 5).

The fluidized material incorporated water ponded along the slope toe, about 400 mm of rainfall in the twenty-one days before the slide, and water that had infiltrated the 2006 landslide derived colluvium. This allowed the colluvial mass to lose significant strength and flow across the river and entraining further quantities of water filled colluvium and river alluvium. This is a similar mechanism proposed by Sassa (1985) for shallow landslides surcharging downslope loose granular soil so rapidly as to cause “impact liquefaction” a process which Sassa (2000) later duplicated in an undrained torsional ring shear apparatus.

Figure 6 shows rafted blocks of unsaturated outwash sands and glacial till from the Whitman Bench traveled to near the alignment of SR530. Conversely, the liquefied colluvium flowed over SR530 and continued for another 0.5 km on the west side of the hill shown in Fig. 6.

Some of the field observations that confirm the fluid nature of the colluvium are piles of rafted outwash sand and overconsolidated glacial till from the Whitman Bench near SR530 and some still upright trees that were carried on top of the rafted sand blocks from top of the slope to south of the river (see Fig. 7). The fluidized colluvium moved farther than the outwash sands from the Whitman Bench (Phase 1), which was riding or rafting along on some of the fluidized colluvium. The rheology of the disturbed colluvium (fluid like) was clearly different from the rheology of the initial Phase I slide mass, which involved unsaturated overconsolidated materials, e.g., outwash sands and glacial till, and remained frictional instead of exhibiting fluid/liquefied behavior.

Phase II Slide Mass

The mobility of the colluvium and Phase I initial slide mass caused unbuttressing of the upper slope, which initiated a retrogression into the intact material of the Whitman Bench. Based on inverse limit equilibrium stability analyses, Fig. 5 shows the probable compound failure surface for the Phase II slide mass that primarily involved the upper portion of the slope. The Phase II slide mass involves unsaturated and intact outwash sands, glacial till, and the upper portion of the Advanced Glacio-Lacustrine clay deposit. The unsaturated portions of the outwash sands and glacial till deposits exhibited frictional behavior which resulted in the formation of large landslide blocks instead of a flowslide as observed in the colluvium. As a result, the Phase II slide mass was much less mobile and is not responsible for any of the property damage or loss of life in the valley. The top of this slide mass forms the new landslide bench (see Fig. 6) that will protect the overlying Whitman Bench for many years to come because the river cannot directly erode this bench or the Upper Plateau due to the lower portion of the Phase II slide mass covering the lower portion of the slope.

Figure 7 shows an aerial photograph of the slope in July 2013, the location of the 2006 headscarp, and the extent of the Phase 1 and 2 slide masses in 2014. The Phase II slide mass primarily involves the Whitman Bench while the Phase 1 slide mass involves part of the Whitman Bench and the slope below the 2006 headscarp. The Phase II slide mass also involves the mature trees that were located on the Whitman Bench prior to the 2014 landslide and are now on the new landslide bench shown in Fig. 6.

Aerial photographs show the Whitman Bench slope remained stable for over one hundred years and LiDAR images of adjacent slopes show similar slopes have remained stable for much longer. However, landslides involving the lower portion of the slope will continue to occur as the river erodes the 2014 landslide debris and undermines portions of the new and still tree-covered landslide bench (see arrow in Fig. 6) but these lower elevation slides will not directly impact the Whitman Bench. Based on river migration and erosion rates calculated for the 1937, 1951, 1952, 1967, 1988, and 2006 landslides, it will take at least 300 years to remove enough of the Phase II slide mass and landslide bench to oversteepen and/or undermine the Whitman Bench sufficiently to cause another large landslide that moves past the river and across the valley as in 2014. This time estimate is based on aerial photographs from 1937, 1951, 1952, 1967, 1988, and 2006 that identified the location of the river at each time so the rate of migration could be estimated using the time between each photograph. As a result, studying the effect of the river on the new landslide bench using LiDAR

images, as shown in Fig. 4, is important to evaluate the landslide hazard and risk with time as discussed below.

Figure 6 shows the Phase II slide mass stretched or spread out as it moved down the slope but did not become highly mobile like the colluvial flowslide. The runout of the Phase II slide mass was limited, because it was mainly frictional and its leading edge collided with the back edge of the Phase I slide mass. On the western end, the Phase II slide mass actually over-rode the northern edge of the Phase I slide mass because some Advanced Glacio-Lacustrine Clay from the Phase II slide mass was found overlying the trees and outwash sands of the Phase I slide mass (see dashed circle in Fig. 6).

Seismic Records

The two-phase failure mechanism described above is also in agreement with nearby seismograph recordings that show two distinct ground motions separated by about two minutes. Figure 8a shows the various ground motion recording stations near the 2014 Oso Landslide. The recording stations designated as JCW, B05A, and CMW are located at distances of approximately 10, 17, and 22 km, respectively, from the 2014 landslide. Figure 8b presents the ground motions from recording station JCW (Jim Creek Wilderness Station at: 48°12'13"N 121°55'00"W). Figure 8b show two distinct ground motions with durations of 96 and 70 s separated by about two minutes.

The first ground motion recording started at 10:37.30 on 22 March 2014 and ended at 10:40.00 while the second motion started at 10:42.00 and lasted only 1.5 min. Hibert et al. (2014) conclude that these ground motions correspond to two separate landslide events (Phase I and II) with the



Fig. 4 Erosion of sandy outwash deposits by Stillaguamish River two months after landslide

Fig. 5 Two-phase failure mechanism prior to 2014 landslide with the Phase I failure surface based on field observations and inverse slope stability analyses at cross-section location shown in Fig. 1

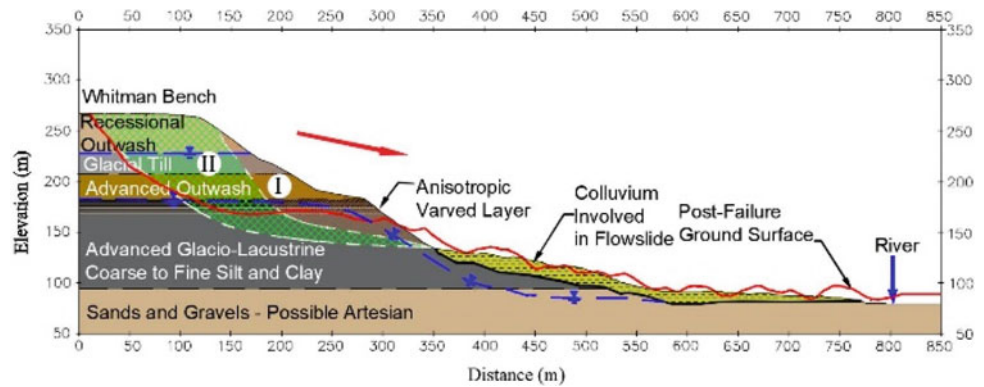


Fig. 6 Aerial view and extent of sand (dashed line) pushing and over-riding fluidized colluvium from slope toe, a new landslide bench (see arrow), and the Phase II slide mass overriding the back end of Phase I slide mass (dashed circle) (image courtesy Rupert G. Tart)

events having different characteristics and runouts. The first ground motion is indicative of a large landslide mass with a velocity and acceleration of 19.4 m/s and 1.0 m/s², respectively (Hibert et al. 2014). This first motion is larger than the second motion and caused the colluvial flowslide. The second ground motion is more impulsive and indicative of a complex breakaway sequence that merged into one landslide (Hibert et al. 2014), which is in agreement with the retrogressive nature of the Phase II slide mass. Because of the fluid nature of the colluvial flowslide, a separate ground motion was not detected for this movement.

Figure 5 illustrates the large slope movements involved in the two-phase failure mechanism, which was initially described in a 1 June 2015 Seattle Times newspaper article (Doughton 2015). The Phase I slide mass moved first with significant speed and momentum, as described by an eyewitness (described below), and impacted the water-filled colluvium that had accumulated along the lower part of the slope. The Phase I slide mass pushed some of the water filled colluvium in front of it across the river, the valley, the unexpected neighborhood, SR530 highway, and beyond. The steep valley slope then remained unsupported and some two minutes later the Phase II slide mass slid down the evacuated slope but did not move far because the materials were primarily unsaturated, dense, and frictional so it stopped at the back edge of the Phase I slide mass.

Unlike other large flow landslides, e.g., La Conchita in 2005, videos of the slide are not available so the proposed failure mechanism may not represent all aspects of the failure mechanism. For example, the geometry of the Phase I slide mass is subjective because the slide mass and scarp were removed. The Phase I slide mass geometry was estimated using results of inverse analyses of the 1967 and 2006 landslides to estimate groundwater and shear strength conditions that were used to predict the 2014 critical compound failure surface shown in Fig. 5.

Runout Analyses

The two-phase failure mechanism shown in Fig. 5. is used below to conduct runout analyses and assess the accuracy of existing runout models. This is important because the failure mechanism is the first and most important input parameter for a runout analysis. If the failure mechanism is incorrect, the runout analysis will not accurately predict the slide mass runout because the kinematics of the slide movement will not be correct.

As a result, the failure mechanism proposed by Stark et al. (2017) is used in the runout numerical models DAN3D,



(a)



(b)



(c)

Fig. 7 Photographs showing: **a** recessional outwash sands and near vertical trees stopped north of SR530, **b** disturbed colluvium in foreground, blocks of outwash sand with trees in valley, and new landslide bench and scarp in background, and **c** nearly vertical tree from upper plateau in Phase I just south of override zone of Phase II

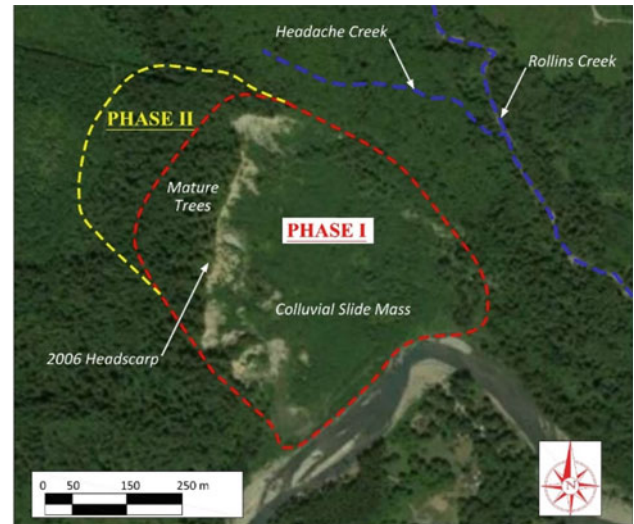
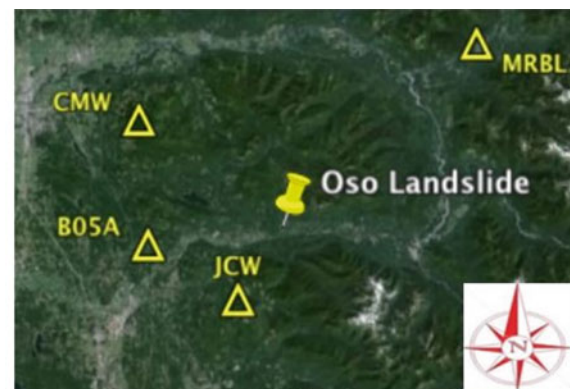
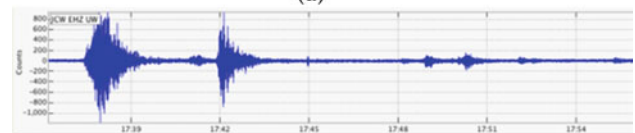


Fig. 8 Aerial view of slope in July 2013 and outline of the 2014 Phase I and II slide masses ((c) 2014 Google)



(a)



(b)

Fig. 9 **a** Aerial photograph from Google Earth showing proximity seismic recording stations to Oso Landslide and **b** ground motions from recording station JCW from Pacific Northwest Seismograph Network

Anura3D, and FLO-2D and the results are compared to field observations made between 22 and 24 May 2014, or about two months after the landslide, by the first author (see Figs. 4 and 7). In particular, the runout results are compared to field observations of the final shape, distance, splash heights, consistency, shear strength, and depth of the slide mass, post-event topography, and ground motions recorded during the two-phase landslide to assess the accuracy of the analyses.

Liquefied Shear Strength

Another important input for the runout analyses is the value of liquefied strength used to model the disturbed water-filled colluvium after being impacted by the Phase I slide mass. This section describes how the liquefied strength was estimated and the value selected for the runout analyses reported herein.

Given field observations of the flow characteristics of the water-filled colluvium (see Fig. 11), the colluvium was modeled using the empirical liquefied strength ratio correlation (Stark and Mesri 1992 and Olson and Stark 2002) developed from earthquake-induced liquefaction flow slides involving contractive granular materials. The field liquefaction case histories analyzed by Stark and Mesri (1992) have an effective overburden stress at the middle of the liquefiable layer that ranges from 0.4 to 5.4 kg/cm² with an average and standard deviation of 1.2 kg/cm² and 1.1 kg/cm². These liquefaction case histories exhibit a range of liquefied strength of 0.02 to 0.33 kg/cm² with an average of 0.11 kg/cm², which is used below for the runout analyses. The liquefied strength applied in the liquefied rheology model was estimated using the following relationship from Stark and Mesri (1992) and Olson and Stark (2002):

$$s_l = 0.033 \text{ to } 0.075 \times (\sigma_v - u) \quad (1)$$

where s_l = liquefied shear strength; σ_v = prefailure total vertical stress; and u = prefailure pore-water pressure. The liquefied strength ratio $s_l/(\sigma_v - u)$, of 0.07 was estimated using a normalized penetration resistance of six as discussed below.

Because the blow count for the heterogeneous water-filled colluvium that flowed past SR530 was not known prior to the 2014 landslide, a representative value was estimated based on field observations by the first author. This resulted in a normalized blowcount of six (6) with the blowcount normalized to an effective vertical stress of 1 kg/cm² (1 tsf) and a standard penetration test energy efficiency of 60%. This resulting value of $(N_1)_{60}$ is six (6) and was used to estimate the liquefied strength ratio of 0.07 from the empirical relationship in Eq. (3) of Olson and Stark (2002).

The liquefied strength ratio of 0.07 was selected for a trial flow analysis, which yielded good agreement with field observations and was not varied in subsequent DAN3D runout analyses even though lowering this ratio may have produced better agreement between the calculated and observed runout on the west side of the slide mass and Engineer Hill as shown below. In fact, the liquefied strength ratio could have been varied from about 0.033 to 0.075 as discussed above to improve the agreement with field observations but was not to evaluate the runout models.

The use of a liquefied strength ratio from earthquake-induced flow slides was first proposed by Oldrich Hungr for a presentation on the 2014 Oso Landslide to the Vancouver Geotechnical Society in Vancouver, British Columbia on 15 April 2015 (Hungr, 2015) with the first author. This is a creative feature of the dynamic analysis presented in Aaron et al. (2017) because this empirical method was developed by Stark and Mesri (1992) for static and seismic flow failures involving saturated, loose granular soils not overconsolidated glacial silts, clays, and till.

The basal resistance used with the liquefied rheology described above does not have an explicit dependence on shear rate, i.e., it is a constant and purely plastic strength. However, the inverse analyses performed by Olson and Stark (2002) includes flow and momentum effects on the liquefied strength. As a result, the expression in Eq. (3) indirectly includes the effects of viscosity and shear rate in the empirical relationship.

DAN3D Results

DAN3D is a depth-averaged numerical solution of the equations of motion in 2D developed by McDougall (2006) and Hungr and McDougall (2009). Depth-averaged means the governing mass and momentum balance equations are integrated and averaged with respect to the depth of predicted flow. The depth-averaged solution, when assuming shallow depth of flow, eliminates the depth-wise dimension (neglecting any shear stress in the depth direction). Thus, the 2D solution corresponds to the model that simulates the motion across a 3D terrain (McDougall 2006). The equations of motion are solved by the smooth particle hydrodynamics solution method (Monaghan 1992).

Additional details of the DAN3D analysis of the 2014 Oso Landslide are described in Aaron et al. (2017). The 2014 Oso Landslide was modeled as two separate events during the DAN3D (Hungr and McDougall 2009) simulation. These two events refer to the movement of the Phase I and Phase II slide masses, respectively, identified by Stark et al. (2017), which is shown in Fig. 5. The DAN3D results show that the Phase I slide mass traveled a long distance and was stopped by Engineer Hill near the center of the runout zone. This protruding area (see “EH” in Fig. 10) consists of slide debris from a historic landslide that initiated on the south side of the valley and moved northward over part of the valley.

The DAN3D Phase I results show good agreement with field observations on the east side of Engineer Hill (EH) but the western portion of the runout zone exhibits a shorter runout than observed. The Phase II slide mass was much less mobile due to its frictional behavior and only moved a short

distance past or south of the Stillguamish River. This runout distance is in agreement with field observations because the downslope end of the Phase II slide mass impacted with the rear of the Phase I slide mass creating an override zone just south of the river (see Fig. 6) and described below.

Figure 6 presents an aerial photograph that shows the Phase II override zone (see dashed red lines) where some of the grey glaciolacustrine silts and clays overrode the trees and recessional outwash sands from the upper plateau or Whitman Bench in Phase I. The DAN3D simulation extends a little past the override zone on the west side but is in good agreement on the east side of the Phase II slide mass. As a result, DAN3D can effectively model the two extremes of slide mass rheology, i.e., fluid flow and frictional, in the runout analysis of the 2014 Oso Landslide. However, DAN3D is not presently commercially available due to the passing of Oldrich Hungr.

ANURA3D Results

This section discusses runout analyses for the 2014 Oso Landslide performed using the Material Point Method (MPM), which is applied generally for the simulation of materials that undergo large and time-dependent deformations (Sulsky et al. 1994). The governing equations are standard mass and momentum conservations in the MPM.

The MPM uses a combination of the Lagrangian and Eulerian descriptions of continuum materials. In an MPM analysis, the materials are represented by a collection of disconnected points and a background computational mesh where the points can move throughout the mesh and carry the material properties assigned from point to point. This information is transferred to the nodes of the mesh, where

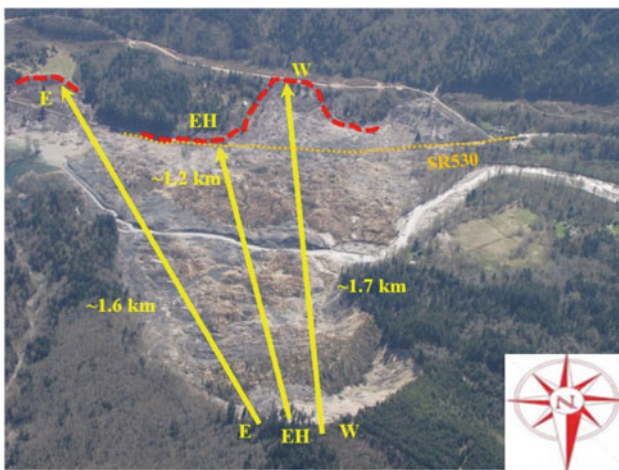


Fig. 10 Aerial view after 2014 landslide showing: observed boundaries of runout (see red dash lines) and travel distances (see yellow solid lines) on both east and west side of Engineer Hill (EH) (image courtesy of Rupert G. Tart and dated 24 March 2014; IMG_5806.jpg)



Fig. 11 Photograph showing Phase I intact grey glaciolacustrine silts and clays and recessional outwash sands behind fluidized colluvium north of SR530

the linear momentum balance equation is solved. The mesh solution then is mapped back to update the information of the material points (Bandara et al. 2016; Bardenhagen et al. 2000).

The nodes of the computational mesh do not retain any data, which means that the mesh itself remains fixed during the analysis but the material points can move to different locations in the computational mesh during the analysis. The computational mesh also facilitates the definition of the analysis boundary conditions.

The MPM is incorporated in the Anura3D software package developed by the MPM research community (Yerro et al. 2018). This software package allows the analysis of displacements along a 2D cross-section of the slope and topography adjacent to the slope consisting of one or two-phase materials. Anura3D does not allow input of a digital terrain model to generate a plan-view of the slide mass runout like DAN3D but the runout can be calculated for each cross-section and plotted on a plan-view as shown below.

The use of a two-phase material model makes it possible to simulate the phase change from solid to fluid, e.g., soil to water, in a fully saturated material. However, only the water-filled colluvium along the slope toe was considered saturated and susceptible to a phase change because the other materials involved in the 2014 landslide are unsaturated, overconsolidated, and not susceptible to a phase change. Representative soil properties were used in Anura3D for the various materials involved to assess the accuracy of the model and not properties that provided the best agreement with field observations.

The stratigraphy, material properties, and two-phase failure mechanism used in the Anura3D model are illustrated in Fig. 12 and shown in Table 1. The residual strength

properties for Slip Zones 2 and 4 were measured using torsional ring shear tests while the other shear strength parameters were estimated.

In the Anura3D analysis, the fixity of the Phase I slide mass is released to initiate the slope movement and runout processes while the Phase II slide mass is kept fixed until runout of Phase I is complete. After the Phase I slide mass stops moving, the Phase II slide mass is then allowed to move by releasing its fixity. This results in the two distinct phases or slide movements being modeled and acting separately. This allows Anura3D to calculate the duration for Phases I and II, which can be compared to the ground motions recorded during the 2014 landslide to investigate the accuracy of the Anura3D model. In addition, the calculated runout distances, slide mass depths, and splash heights are compared with field observations to assess the accuracy of the Anura3D model below.

Anura3D allows the analysis of displacements only along a 2D cross-section not over a digital terrain model. As a result, the analysis conducted herein used three cross-sections to calculate the runout distance and behavior of the slide mass east and west of Engineer Hill and across Engineer Hill (see Fig. 8). Afterwards, the results from these three cross-section are compared to the runout observed at these locations to assess the accuracy of the MPM.

Figure 13 shows the simulation results at time steps of 0, 8, 24, 28, 80, and a total of 138 s, i.e., 80 s for Phase I and 58 s for Phase II, for the western cross-section shown in Figs. 10 and 12. The results illustrate that the Phase I slide mass moved down slope and started impacting the water-filled colluvium within eight seconds of the release of the Phase I slide mass in the model. At eight seconds, the now disturbed or impacted water-filled colluvium is assigned a liquefied strength and it is pushed across the river and flows as a near liquid across most of the valley. This flow behavior continues until 80 s of total elapsed time and the unsaturated materials near the top of the Phase I slide mass are able to travel about 1.2 km in this short period of time (80 s). A distance of 1.2 km is shorter than the observed final runout of the colluvium of about 1.7 km on the west side of Engineer Hill because the unsaturated material of the

upper slope did not travel as far as the water-filled colluvium. These numerical results are consistent with field observations that the intact glacial materials of the upper part of the slope stopped just north of the SR530 at $t_1 = 80$ s. Therefore, Anura3D reasonably predicts the runout of the unsaturated glacial materials as they were transported on the water-filled colluvium across part of the valley. This is significant because it suggests that Anura3D can simulate entrainment of slide material.

The cross-section after twenty-four seconds of slide movement shows a splash of colluvium occurring on the north side of the river, which decreases in height as it continues across the river. These results also match field observations of slide debris and tree damage occurring as high as 10 m in trees just on the southside of the river near the western edge of the slide mass. The field observations show a splash height of over 12 m west of the cross-section analyzed and west of the main direction of runout. As result, it is reasonable that the splash height observed is less than that calculated by Anura3D, which shows a splash height of about 30 m just past the river at a time of 28 s (see Fig. 13).

The splash height of 30 m estimated by Anura3D is more consistent with an eyewitness account by John Reed reported in the Seattle Times that estimated the splash height in the direction of runout of about 30 m:

... When it hit the water, it shot way up, way taller than the tallest trees,” Reed said. “Then I saw this big black wall—it must have been more than 100 feet (30 m) high—rise high above the (Steelhead Drive) neighborhood. The houses, in comparison, looked minuscule. It was unbelievable.... John Reed; (Seattle Times, 3/27/14, https://old.seattletimes.com/html/localnews/2023709258_mudslideedge1.xml.html).

After 80 s of slide movement, runout of the Phase I slide mass converges and essentially stops. It takes about 58 s after the stoppage of Phase I (80 s) for the Phase II slide mass to complete runout for a total runout time of about 138 s. Figure 13 shows at the end of the simulation, the maximum calculated runout on the western cross-section is about 1.5 km, which is in good agreement with field observations of about 1.7 km on the west side of Engineer Hill.

Movement of the Phase II slide mass after 58 s also includes the downslope portion overriding the rear of the Phase I slide mass. After 58 s, the new landslide bench is visible in the upper part of the slope (see Fig. 13 at $t_2 = 58$ s). All of these runout and slide behavior characteristics are consistent with field observations.

The cross-section and surface topography for the eastern cross-section are similar to the western cross-section (see Fig. 13 at t_1 at 0 s). As a result, the east cross-section is not presented herein before discussing the results in this paragraph. In the eastern cross-section, the Phase I slide mass also reached the river after about twenty-four seconds of

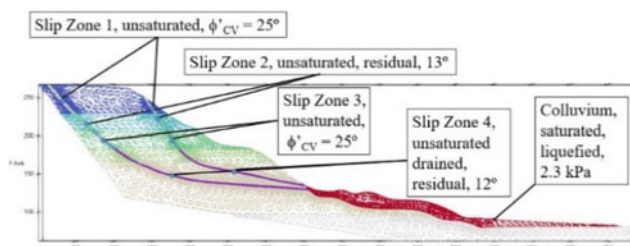


Fig. 12 Slope stratigraphy and failure surfaces for Anura3D runout model

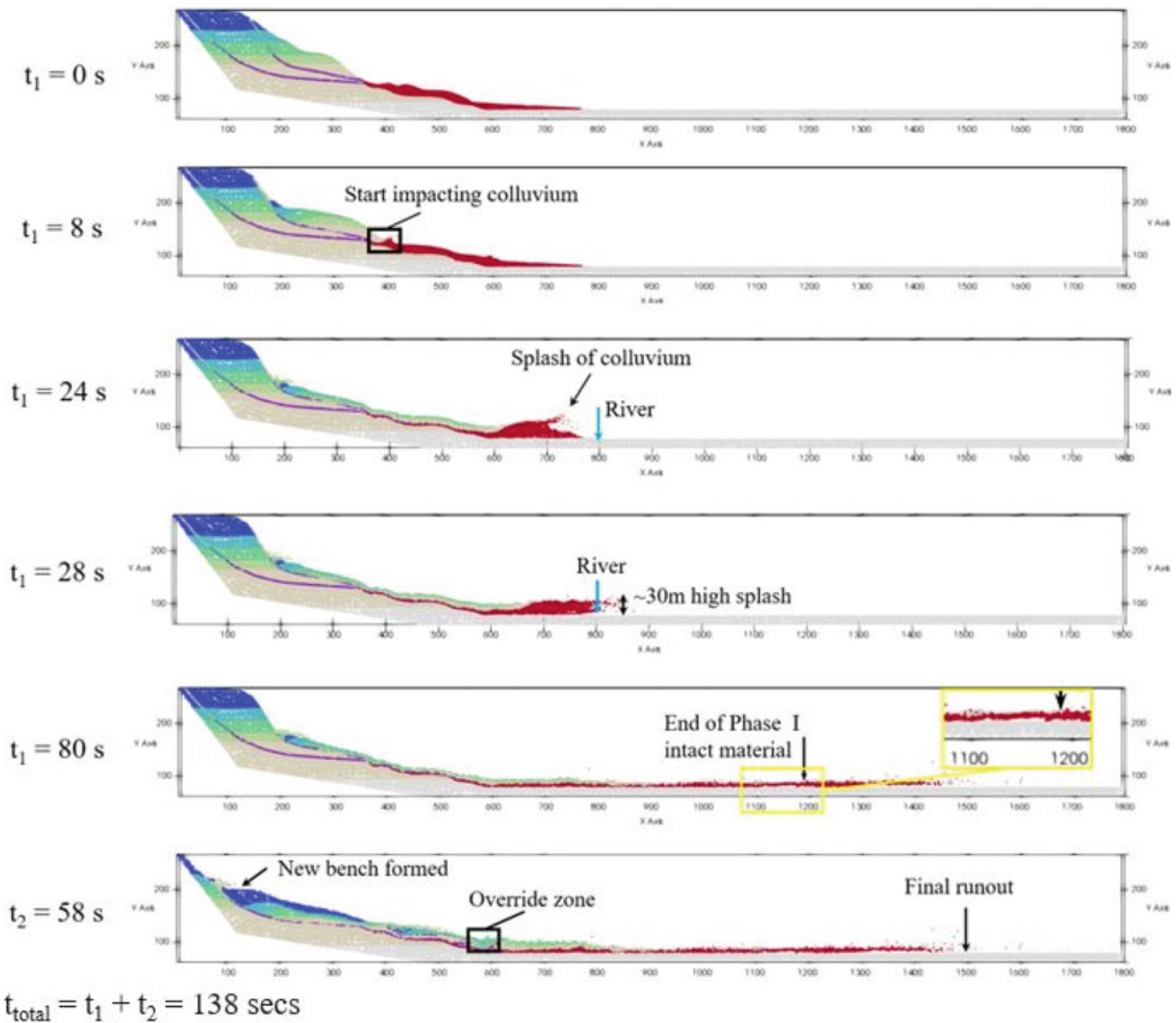


Fig. 13 Anura3D runout behaviors for west cross-section at time steps of: 0, 8, 24, 28, 80, and a total of 138 s in Phases I and II (80 + 58 s)

movement and splashes to a height of about 30 m on the east side of the slide mass. This calculated splash height of 30 m is comparable to that observed in trees along the eastern side of the slide mass given the height of the tree base above the evacuated area. The small calculated splash height of about 5 m along the eastern boundary of the slide mass near SR530 is also in agreement with field observations that show a similar splash height at this distance and a slide mass depth of only about 5 m. In summary, the Anura3D results for the eastern cross-section are in agreement with the observed splash heights and slide mass depths along the eastern cross-section.

Given the similarities between the east and west cross-sections and the topography south of the river prior to movement, the east cross-section also produced a runout of

about 1.5 km. This is also in excellent agreement with the observed runout on the east side of Engineer Hill. Coincidentally, DAN3D also provided excellent agreement with the observed runout on the east side of Engineer Hill. However, DAN3D did not provide a good runout prediction on the west side (too short) of Engineer Hill while Anura3D did provide good agreement on the west side. It is anticipated that the DAN3D analyses would have been in better agreement if the liquefied strength ratio was lowered but it was decided not to change the original ratio of 0.07 estimated by Professor Oldrich Hungr (Aaron et al. 2017). In summary, DAN3D and Anura3D provided good predictions of the observed runout with Anura3D giving better agreement on both the east and west sides and the top of Engineer Hill as discussed in the next paragraph. The results for the

cross-section that passes through Engineer Hill (see Fig. 10) are also interesting because a splash height was observed in some of the trees on top of Engineer Hill. The top of Engineer Hill is about 16 m above the SR530 pavement and there was slide debris on and damage to trees on top of Engineer Hill about 3 m above the ground surface. The force of the slide mass was evident by the presence of at least one vehicle being pushed to the top of Engineer Hill.

The Anura3D simulation results for the Engineer Hill cross-section show at a time step of 42 s the Phase I slide mass reach Engineer Hill and causes a splash of about 20 m. Given the top of Engineer Hill is about 16 m above the pavement of SR530, a total splash height of about 20 m is in agreement with observations of slide debris on and damage to trees at a height of about 3 m above pre-existing ground on top of Engineer Hill for a total splash height of about 19 m. This agreement between field observations and calculated runout reinforces the usefulness of the Anura3D analysis.

The final runout topography from Anura3D was compared with slide mass depths derived from subtracting the 2006 and 2014 LIDAR images. The two topographies compare well except for the upper portion of the slope, which indicates lower mobility of the Phase II slide mass than actually observed. Several factors may result in this Phase II difference, which include the ground motions that were recorded (see Fig. 9b) were not modeled in the Anura3D analysis, which can impact the kinematics of the flow failure, simplifications used to model the complex subsurface conditions involved in the 2014 landslide, and estimating the effective stress parameters for the outwash sand layers and glacial till at the top of the slope because these materials were not tested by Stark et al. (2017).

Another means to verify the accuracy of the Anura3D model and runout prediction is to compare the duration of the simulated Phase I and II runouts with the ground motions recorded during the 2014 landslide. For example, the ground motions recorded at station JCW during the 2014 Oso landslide on 22 March 2014 show the ground velocity time histories for the two phases of slope movement have durations of 96 and 70 s for Phases I and II, respectively, (see Fig. 8b). These two ground motions are separated by about 162 s of quiet or no significant ground motion. This quiet period cannot be modeled in Anura3D because the Phase II slide mass does not start moving until its fixity is removed by the user. The fixity can be removed after 162 s manually but it is not released by Anura3D to simulate the kinematics of the actual failure. The observed durations of slope movement of 96 and 70 s are a little greater than the Anura3D durations of 80 s for Phase I and 58 s for Phase II but these durations are in reasonable agreement.

In summary, Anura3D provided a good simulation of the runout behavior of the 2014 Oso Landslide, i.e., runout

distance, splash height, slide mass depth, and duration on the west side of Engineer Hill, using field representative input parameters. This bodes well for use of Anura3D to predict runout of other slopes along the Stillaguamish River Valley.

FLO-2D Results

FLO-2D is a 2D finite difference model that simulates non-Newtonian floods and debris flows. FLO-2D was developed by O'Brien et al. (1993) and uses fluid behavior to predict runout behavior. The model adopts the continuity equation and 2D equations of motion to govern the constitutive behavior of a fluid. In a debris flow analysis, sediment-involved flows with high volumetric concentration are treated as homogeneous fluid based on Peng and Lu (2013). By inputting a digital elevation model to define the ground surface topography of the analysis area, the fluid flows along the terrain low spots and the range of runout can be predicted.

The following three factors dominate the behavior of the flowing materials in this rheology analysis: (i) yield stress, (ii) viscosity, and (iii) influence of turbulence and dispersion on flow. An expression of the total shear stress mobilized in the hyper-concentrated flow incorporating these three factors is given by the following equation from O'Brien and Julien (1988):

$$\tau = \tau_y + \eta \left(\frac{dv}{dy} \right) + C \left(\frac{dv}{dy} \right)^2 \quad (1)$$

where τ_y is the yield stress that is required to trigger the flow of the sediments, η is the viscosity of the sediment during flow, C is the inertial shear stress coefficient, and $\frac{dv}{dy}$ is the rate of shearing strain in flow. The sum of first two terms in Eq. (1) is the shear stress assumed in the Bingham plastic rheology model (Schamber and MacArthur, 1985; O'Brien, 1986), which introduces a linear stress-strain relationship. Normally Bingham fluid behavior applies to hyper-concentrated flow of clay and quartz particles in water under low shearing rates (Govier and Aziz, 1982).

The viscosity and yield stress in Eq. (7) are determined using the following empirical correlations:

$$\eta = \alpha_1 e^{\beta_1 C_v} \quad (2)$$

$$\tau_y = \alpha_2 e^{\beta_2 C_v} \quad (3)$$

where α_i and β_i are empirical coefficients and C_v is the sediment concentration by volume not mass. A rheology model that incorporates the three factors above, i.e., yield stress, viscosity, and turbulence and dispersion on flow, enables FLO-2D to simulate a variety of flooding and debris flow problems.

To be implemented in FLO-2D, the total shear stress expression in Eq. (1) is depth-integrated and rewritten in slope form as presented in O'Brien and Julien (1993). A rheology model that incorporates the three factors above, i.e., yield stress, viscosity, and turbulence and dispersion on flow, enables FLO-2D to simulate a variety of flooding and debris flow problems.

O'Brien et al. (1993) obtained empirical coefficients for several different mudflow matrices through laboratory tests, which are referred to herein for determination of the yield stress and viscosity factors to model mudflow materials. The properties of water-filled colluvium are closest to those of the Aspen Pit I mudflow materials (see O'Brien et al. 1993) based on comparison of index properties, e.g., liquid limit and clay-size fraction of 0.32 and 31%, respectively.

According to the flow properties of the Aspen Pit I mudflow summarized by O'Brien et al. (1993), $\alpha_1 = 0.036$, $\beta_1 = 22.1$, $\alpha_2 = 0.181$, and $\beta_2 = 25.7$ are used for the water-filled colluvium in the FLO-2D analysis herein. The yield stress and viscosity are also sensitive to the sediment concentration. As the volumetric sediment concentration varies from 0.1 to 0.4, the values of these two factors can be changed by three orders of magnitude (O'Brien et al. 1993). Considering a porosity of 0.61 for the water-filled colluvium based on a saturated unit weight of 16.5 kN/m^3 , the volumetric sediment concentration is taken to be 0.39. Subsequently, the yield stress and viscosity can be calculated through Eqs. (2) and (3), respectively.

An advantage of the FLO-2D software package over the Anura3D package is a digital terrain model (DTM) can be imported to initialize the FLO-2D analysis. The rupture surface for the Phase I slide mass is then added to the DTM to define the volume of the Phase I slide mass as the volume of material between the rupture and ground surfaces. The evacuation zone for the Phase I slide mass is obtained by subtracting the post-Phase I topography from the pre-event topography. On the basis of the DTM, grids with a size of 50 m by 50 m were created and elevation points were interpolated to discretize the slide mass. In the FLO-2D analysis, only the water-filled colluvium in Phase I is assumed to flow like a liquid during the simulation. Thus, flow input parameters were only assigned to grids corresponding to the initial location of water-filled colluvium.

The hydrograph at each grid, reflecting the change of flow volume with time, is assumed to be triangular-shaped (Wanielista 1990; Coroza et al. 1997; SWCB 2008; Li et al. 2010; Croke et al. 2011; Peng and Lu 2013) for simplification. Thus, the input source of flow debris linearly increases from zero to a peak and then linearly decreases to zero at each grid. These increases and decreases are occurring over each time step, which is 0.1 s for the analyses performed herein. The peak of discharge is determined by the grid area and average colluvium thickness in the

corresponding grid, and the assumed time span of 60 s is comparable to the main portion of the first recorded event duration.

The FLO2D runout (blue) is compared to the actual (orange) and DAN3D (green) runout zones in Fig. 14. In particular, Fig. 14 shows the FLO-2D analysis significantly under predicts the runout on the east side of Engineer Hill and the largest portion of the runout goes towards the west along the channel of the Stillguamish River. The runout goes primarily west along the river channel because of the decrease in elevation of the channel instead of across the river valley. This is due to FLO-2D only allowing surface topography to influence flow direction and distance instead of potential energy or kinematics of the slide mass as discussed below.

In an effort to improve the runout prediction by FLO2D, the water-filled colluvium was modeled as water in a subsequent analysis instead of a soil. Using the flow properties of water, reduces the resistance of the colluvium to flow and should yield a larger runout zone than the first analysis that utilized mudflow properties for the colluvium. It was anticipated that this analysis might give better agreement with the observed runout and is the best chance of improving the comparison between FLO-2D and field runout observations. The results of the FLO-2D runout analysis that uses water, i.e., little flow resistance, for the water-filled colluvium is shown in Fig. 14. The revised FLO-2D runout (see light blue area) is compared to the actual (orange) and DAN3D (green) runout zones in Fig. 14. This comparison still shows the largest portion of the runout going towards the west along the river channel and still does not provide a good estimate of the actual runout even assuming the colluvium has the resistance of water. As a result, it is concluded that FLO-2D

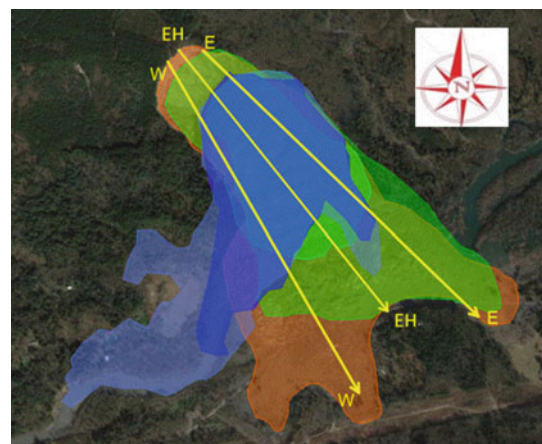


Fig. 14 Comparison of runout zones for: FLO-2D using mudflow properties (see dark blue area) and water for the colluvium (light blue area), DAN3D (green area), Anura3D (yellow lines), and observed impact zone (orange area)

is best suited for situations where only topography, not slide mass potential energy or kinematics, controls slide mass runout.

In Fig. 14 the DAN3D results include both Phases I and II with Phase I being darker green in color than Phase II, which stops just south of the river. The DAN3D results are in excellent agreement with field observations on the east side of Engineer Hill and a little short of the observed runout on the west side of Engineer Hill. The DAN3D results are also in excellent agreement with the runout reaching Engineer Hill in the middle of the debris field and causing some splashing on the top of the hill. The Anura3D runout results east and west of Engineer Hill are in good agreement with field runout observations (orange) but the results are only available for the three cross-sections analyzed.

FLO-2D does provide a better estimate of the runout zone in the westernmost portion of the landslide than DAN3D but this does not compensate for the great deviation from field observations in other portions of the slide mass. Anura3D does not provide an estimate of the influence zone if a cross-section is not drawn in the desired area so its results also have some limitations.

In summary, FLO-2D is able to provide a preliminary estimate of the runout or impact zone of a flood or fluid flowslide. However for planning and risk assessment activities, the FLO-2D results should be supplemented or replaced by another runout analysis, e.g., DAN3D and/or Anura3D, to capture the effect(s) of slope potential energy and kinematics to accurately predict runout and risk to infrastructure and public safety.

Summary

This paper summarizes the slope history, investigation, and analyses used to determine the two-phase failure mechanism of the 22 March 2014 landslide near Oso, Washington that destroyed more than 40 homes and fatally injured 43 people and the accuracy of available runout analyses to simulate the observed behavior. The key findings are:

- The 2014 landslide occurred in two phases with Phase I consisting of an initial landslide involving the Upper Plateau, i.e., Whitman Bench, that was over-steepened by the 2006 landslide. Phase II is a retrogressive landslide in the Upper Plateau caused by evacuation of the Phase I slide mass, which left the upper terrace unbuttressed.
- Rainfall in the 21 days before the 2014 landslide is the wettest on record and corresponds to a 97-year return period and contributed to initiation of the Phase I landslide on the eastern end of the ancient landslide bench.

- Slope toe erosion by the Stillguamish River did not contribute to initiation of the Phase I landslide because it had been pushed south by the 2006 landslide.
- The Phase I landslide impacted, pushed, and over-rode the water filled, disturbed, and softened colluvium along the slope toe, causing a large undrained strength loss similar to the mechanism proposed by Sassa (1985 and 2000) that enabled the colluvium to flow about two km across the valley and carry the recessional outwash sands and trees from the upper plateau across part of the valley.
- Phase II did not exhibit a large runout because the materials are overconsolidated, unsaturated, frictional, and were stopped by the back of the Phase I slide mass.
- Future LiDAR hazard mapping should identify the following two areas because they pose a high risk of a large runout across the valley floor: (1) slopes that have been oversteepened and/or undermined by prior sliding, river erosion, and/or other landslide activity, e.g., see adjacent landslides in Fig. 3, and (2) areas that are not steep over the entire slope length because of a significant accumulation of colluvium along the slope toe and do not exhibit an ancient landslide bench sufficiently wide to support the Upper Plateau, e.g., 2014 landslide. Therefore, slope height alone is not a good indicator because many other slopes along this river valley have a similar or greater height than the 2014 landslide but have a slope profile, i.e., ancient landslide bench, that is sufficient to maintain stability of the Upper Plateau or Whitman Bench.
- The runout results from DAN3D and Anura3D are in good agreement with field observations in respect to the final distance traveled, post-event topography or slide mass depth, observed splash heights, and duration of each phase of slope movement.
- It is recommended that a range of liquefied strength ratio be used for the runout analyses to bracket the range of runout and impact to infrastructure and public safety for risk assessments.
- The runout analysis performed using FLO-2D is not in agreement with field observations because the code utilizes a fluid flow model so the slide mass primarily follows the low spots in the ground surface topography and the effects of slide mass potential energy and kinematics are not incorporated. The potential energy of the Phase I slide mass caused the water-filled colluvium along the slope toe to be pushed across the Stillguamish River and undergo a large undrained strength loss, which is not modeled in FLO-2D. As a result, FLO-2D significantly under predicted the runout zone of the 2014 slide mass.

Data Availability Statement

Some or all data, models, or code generated or used during the study are available from the first author by request.

Acknowledgements The first author appreciates the financial support of the National Science Foundation (NSF Award CMMI-1562010). The contents and views in this paper are those of the individual authors and do not necessarily reflect those of the National Science Foundation or any of the represented corporations, contractors, agencies, consultants, organizations, and/or contributors mentioned or referenced in the paper.

References

- Aaron J, Hungr, O, Stark TD, Baghdady AK (2017) Oso, Washington, Landslide of March 22, 2014: dynamic analysis. *J Geotechn Geoenviron Eng* 143(9):05017001-1–05017001-13
- Badger TC, D'Ignazio M (2018) First-time landslides in vashon advance glaciolacustrine deposits, Puget Lowland, U.S.A. *Eng Geol* 243:294–307
- Bardenhagen SG, Brackbill JU, Sulsky D (2000) The material-point method for granular materials. *Comput Methods Appl Mech Eng* 187(3–4):529–541
- Bandara S, Ferrari A, Laloui L (2016) Modelling landslides in unsaturated slopes subjected to rainfall infiltration using material point method: modelling landslides in unsaturated slopes subjected to rainfall infiltration using material point method. *Int J Numer Anal Meth Geomech* 40(9):1358–1380
- Cao Q, Henn B, Lettenmaier DP (2014) Analysis of local precipitation accumulation return periods preceding the 2014 Oso mudslide. Department of Civil and Environmental Engineering, University of Washington, Seattle
- Coroza O, Evans D, Bishop I (1997) Enhancing runoff modeling with GIS. *Landscape Urban Plan* 38:13–23
- Croke BFW, Islam A, Ghosh J, Khan MA (2011) Evaluation of approaches for estimation of rainfall and the unit hydrograph. *Hydrol Res* 42(5):372–385
- Doughton S (2015). Laser map gave clue to Oso slide's ferocity. <https://www.seattletimes.com/seattle-news/science/laser-map-gave-clue-to-oso-slides-ferocity/>. June 2, 2015
- Govier GW, Aziz K (1982) The flow of complex mixtures in pipes. Krieger Publishing Co., Melbourne, Fla
- Hibert C, Stark CP, Ekstrom G (2014) Seismology of the Oso-Steelhead Landslide. *Nat. Hazards Earth Syst Sci Discuss* 2:7309–7327
- Henn B, Cao Q, Lettenmaier DP, Magirl CS, Mass C, Bower JB, St. Laurent M, Mao Y, Perica S (2015) Hydroclimatic conditions preceding the March 2014 Oso landslide. *J Hydrometeorol* 16(3):1243–1249
- Hungr O, Leroueil S, Picarelli L (2014) The Varnes classification of landslide types, an update. *J Landslides* 11(2):167–194
- Hungr O, McDougall S (2009) Two numerical models for landslide dynamic analysis. *Comput Geosci*. 35(5):978–992
- Hungr O (2015) "Non-textbook Flowslides in Fine-grained Colluvium" presentation to the Vancouver Geotechnical Society, Vancouver, British Columbia, April 15, 2015. https://hkustconnect-my.sharepoint.com/:b/g/personal/zxubv_connect_ust_hk/EccZwLaKFGxAoFdh-IQ7TLEBm9XVv6tcGD-nSD8yr-N_kQ?e=FYJmZa
- Iverson RM, George DL, Allstadt K, Reid ME, Collins BD, Vallance JW, Bower JB (2015) Landslide mobility and hazards: implications of the 2014 Oso disaster. *Earth Planet Sci Lett* 412:197–208
- Keaton JR, Wartman J, Anderson S, Benoit J, deLaChapelle J, Gilbert RB, Montgomery DR (2014) The 22 March 2014 Oso landslide, snohomish county, Washington. Geotechnical Extreme Event Reconnaissance (GEER), National Science Foundation, Arlington, VA, p 186
- Kim JW, Lu Z, Qu F, Hu X (2015) Pre-2014 mudslides at Oso revealed by InSAR and multi-source DEM analysis. *J Geomat Nat Hazards Risk* 6(3):184–194
- Li CC, Lin A, Tsai YJ (2010) A study of the sediment problem caused by typhoon morakot—taking the watershed of tsengwen reservoir as an example. *J Taiwan Disaster Prevent Soc* 2(1):51–58
- McDougall S (2006) A new continuum dynamic model for the analysis of extremely rapid landslide motion across complex 3D terrain. Ph. D. thesis, University of British Columbia, Vancouver, BC, Canada
- Monaghan J (1992) Smoothed particle hydrodynamics. *Ann Rev Astron Astrophys* 30(1):543–574
- O'Brien JS (1986) Physical processes, rheology and modeling of mudflows. Ph.D. thesis, Colorado State University, Fort Collins, Colo
- O'Brien JS, Julien PY (1988) Laboratory analysis of mudflow properties. *J Hydraulics Eng ASCE* 114(8):877–887
- O'Brien JS, Julien PY, Fullerton WT (1993) Two-dimensional water flood and mudflow simulation. *J Hydraulic Eng* 119(2):244–261
- Olson SM, Stark TD (2002) Liquefied strength ratio from liquefaction flow failure case histories. *Can Geotech J* 39(3):629–647
- Peng SH, Lu SC (2013) FLO-2D simulation of mudflow caused by large landslide due to extremely heavy rainfall in southeastern Taiwan during typhoon morakot. *J Mt Sci* 10(2):207–218
- Sassa K (1985) The mechanism of debris flow. In: Proceedings of XI international conference on soil mechanics and foundation engineering (SMFE), vol 2, CRC Press, Taylor & Francis Group, Boca Raton, FL, pp 1173–1176
- Sassa K (2000) Mechanism of flows in granular soils. In: Proceedings of international conference of geotechnical and geological engineering, GEOENG 2000. Melbourne, vol 1, pp 1671–1702
- Schamber DR, MacArthur RC (1985) One-dimensional model for mudflows. In: Proceedings of ASCE specialty conference on hydraulics and hydrology in the small compute age, vol 2, pp 1334–1339
- Shannon WD, Associates (1952) Report on slide on north fork stillaguamish river near Hazel, Washington, unpublished report to the State of Washington Departments of Game and Fisheries, p 18
- Stark TD, Baghdady AK, Hungr O, Aaron J (2017) Case study: Oso, Washington, landslide of March 22, 2014—material properties and failure mechanism. *J Geotechn Geoenviron Eng* 143(5), 05017005-1–05017001-10
- Stark TD, Mesri G (1992) Undrained shear strength of liquefied sands for stability analysis. *J Geotechn Eng* 118(11):1727–1747
- Sulsky D, Chen Z, Schreyer HL (1994) A particle method for history-dependent materials. *Comput Methods Appl Mech Eng* 118(1–2):179–196
- Sun Q, Zhang L, Ding X, Hu J, Liang H (2015) Investigation of slow-moving landslides from ALOS/PALSAR images with TCPInSAR: a case study of Oso, USA. *J Remote Sens* 7:72–88
- SWCB (2008) Integrated watershed investigation and planning manual. Report of Soil and Water Conservation Bureau, Council of Agriculture, Chinese Taipei
- Thorsen GW (1969) Landslide of January 1967 which diverted the North Fork of the Stillaguamish River near Hazel, Memorandum dated November 28, 1969. to Marshall T. Hunting, Department of Natural Resources, Geology and Earth Resources Division, Olympia, WA
- Wanielista MP (1990) Hydrology and water quantity control. John Wiley and Sons Publishing, New York, USA, p 230

-
- Wartman J, Montgomery DR, Anderson SA, Keaton JR, Benoit J, de la Chapelle J, Gilbert RB (2016) The 22 march 2014 Oso landslide, Washington, USA. *J Geomorphol* 253:275–288
- Yerro A, Soga K, Bray J (2018) Runout evaluation of Oso landslide with the material point method. *Can Geotechn J* 1–14. <https://doi.org/10.1139/cgj-2017-0630>